Energy 350 (2026) 140718

Contents lists available at ScienceDirect

Energy

journal homepage: www.elsevier.com/locate/energy

Thermodynamic analysis and optimization of integrated spectral-beam-splitting photovoltaic-thermal and organic flash cycle system

Yucheng Fang [a], Chao Xu [b], Jinliang Xu [a,b], Zheng Miao [a,b,*]

[a] The Beijing Key Laboratory of Multiphase Flow and Heat Transfer, North China Electric Power University, 102206, Beijing, China
[b] Key Laboratory of Power Station Energy Transfer Conversion and System (North China Electric Power University), Ministry of Education, 102206, Beijing, China

ARTICLE INFO

Keywords:
Combined heat and power
Spectral-beam-splitting
Solar energy
Organic flash cycle
Concentrated photovoltaic-thermal

ABSTRACT

The spectral-beam-splitting concentrating photovoltaic-thermal (SBS-CPV/T) system has attracted increasing research interest for its flexibility in adjusting the solar energy distribution among photovoltaic and photothermal units and its high utilization of solar radiation. A novel system integrating the SBS-CPV/T system and the organic flash cycle (OFC) directly through the nanofluid is proposed in this work for higher solar energy utilization efficiency in combined heat and power systems. This configuration converts the indirect heat supply of the heat exchanger between the heat source and OFC into the direct replenishment of heat using nanofluids. The thermodynamic model of the SBS-CPV/T-OFC system is established, and the effects of four different OFC configurations and key parameters are explored. The electrical efficiency of the SBS-CPV/T system can reach 11.79% while the thermal efficiency is 28.19%. The optical loss is the main energy loss in the SBS-CPV/T system. A higher outlet temperature of the heat collection tube and an appropriate flashing pressure after the throttle valve lead to better performance of the OFC systems. The regenerative double flashing OFC (RDOFC) shows the highest exergy efficiency of 53.52% under a solar irradiance of 1000 W/m^2, which is 9.6% higher than that of the basic OFC (BOFC). The SBS-CPV/T-RDOFC system with R1336mzz(Z) as the recommended working fluid achieves electrical efficiency and thermal efficiency up to 15.49% and 51.87%, respectively.

Nomenclature

Abbreviation		I	exergy destruction, W
BOFC	basic OFC	m	mass flow rate, kg/s
CON	condenser	P	pressure, kPa
CP	conductive plate	Q	energy, W
CPV/T	concentrating photovoltaic-thermal	s	specific entropy, J/(kg·K)
DOFC	double-flashing OFC	T	temperature
EXP	expander	W	power, W
FT	flash tank		
GWP	global warming potential	*Greek symbols*	
HCT	heat collection tube	α	absorptivity
HE	heat exchanger	β	solar cell temperature coefficient
HTF	heat transfer fluid	γ	shadowless PTC region coefficient
$I_{AM1.5}$	air mass 1.5 spectral irradiance	η	efficiency
NNF	nanofluid	λ	wavelength
NNP	nanoparticle	ρ	reflectivity
ODP	ozone depletion potential	τ	transmissivity

(*continued on next column*)

(*continued*)

OFC	organic flash cycle		
ORC	organic Rankine cycle	*Subscripts*	
PTC	parabolic trough concentrator	0	ambient conditions
RDOFC	regenerative double-flashing OFC	con	condenser
ROFC	regenerative OFC	cw	cooling water
SBS	spectral beam splitting	el	electricity
SC	security classification	ex	exergy
SR	spectral response	exp	expander
TV	throttle valve	gt	glass tube
		net	net power
Symbols		nnf	nanofluid
E	exergy, W	std	standard
h	specific enthalpy, J/kg	th	thermal

1. Introduction

The environmental pollution caused by fossil fuel utilization prompts

* Corresponding author. The Beijing Key Laboratory of Multiphase Flow and Heat Transfer, North China Electric Power University, 102206, Beijing, China.
E-mail address: miaozheng@ncepu.edu.cn (Z. Miao).

https://doi.org/10.1016/j.energy.2026.140718
Received 11 December 2025; Received in revised form 25 February 2026; Accepted 10 March 2026
Available online 12 March 2026
0360-5442/© 2026 Elsevier Ltd. All rights are reserved, including those for text and data mining, AI training, and similar technologies.

researchers to explore renewable energy [1–5]. Solar energy, which is a widely distributed, substantial, and environmentally friendly energy source, is regarded as a significant alternative to fossil fuels and has been extensively utilized around the world in recent years. The two most general methods of utilizing solar energy, photovoltaic (PV) and photothermal technologies, can satisfy the major energy demands of domestic life and industrial production and greatly reduce carbon emissions [6,7]. Due to the excellent performance of photovoltaic-thermal (PV/T) hybrid systems in practical applications, they have attracted the interest of many researchers over the past few decades.

Generally, in PV/T systems, researchers adopt spectral beam splitting (SBS) technologies to achieve higher utilization efficiency of solar energy [8,9]. It can help the heat transfer fluid (HTF) acquire a higher outlet temperature without unnecessary loss of electrical efficiency [10]. Commonly, the SBS technique in the PV/T system can be mainly realized in two ways: the reflection-beam-splitting method based on optical films [11–13] and the absorption-beam-splitting method based on nanofluid [14,15]. The reflection-beam-splitting method based on optical films not only offers advantages such as high spectral beam-splitting efficiency and long service life, but also has the drawbacks of high initial investment cost, the complicated production process of optical films, and difficulty in accurately controlling the angle of incidence of light [16]. Compared with the former, the absorption-beam-splitting method based on nanofluid utilizes the nanofluid characteristics of high transmission and high absorption of solar radiation in specific wavelength bands to realize the SBS in the PV/T system [17]. It converts solar radiation that cannot be used for photovoltaic conversion into heat by direct absorption and acts as a heat transfer and storage working fluid, which reduces heat loss significantly due to multiple heat exchanges [18,19]. Moreover, it is easy to adjust the type, size, concentration, and base fluid of nanofluids, and the properties of nanofluids are affected by these factors [16,20,21], so that the most suitable combination between PV cells and nanofluids can be selected for practical applications in the SBS-PV/T systems. It is worth noting that the absorption-beam-splitting method based on nanofluid currently faces difficulties, such as the need for reasonable structural design and higher maintenance costs during the operation of the system.

To further enhance system performance, researchers have investigated the effects of different materials [22–24] and system structures [25–28] in the SBS-PV/T systems. Govind et al. [29] designed an unglazed PV/T system with a sheet configured with a serpentine coil, which used the water and copper oxide-based nanofluid as the heat recovery fluid. The average electrical efficiency of the system was increased by 35.67% in comparison to the uncooled PV/T system. Hussein et al. [30] tested a water-based and a Silicon Carbide nanofluid in the PV/T systems to obtain experimental data of the performance enhancement in PV/T power production and found that the electrical efficiency increased by 8.51% and 20.21% for the water-based and nanofluid-based PV/T systems, respectively. Regarding structural optimization of SBS-PV/T systems, Liu et al. [31] researched the inner fin width, number of cross-sections, height, and number of intervals of fins in the PV/T system and evaluated the effects of these four factors on the system performance. The optimal parameters demonstrated that the thermal efficiency and electrical efficiency were enhanced by 12.28% and 1.31%, respectively. Ma et al. [32] proposed a novel application of a triangular cooling duct in the SBS-PV/T system. Their results showed that the total system efficiency with the triangular receiver is 7.9% higher than that with the flat-plate receiver under the same operating parameters.

From the works mentioned above, it can be observed that the analysis and optimization of SBS-PV/T systems based on nanofluids is relatively sufficient. However, the higher conversion efficiency of renewable energy into electricity is expected to be realized so that it can be widely utilized [33]. Therefore, researchers combine the organic Rankine cycle (ORC) and the SBS-PV/T system to recycle low-grade waste heat more efficiently [34,35]. Kiyarash et al. [36] combined the solar concentrating devices that utilized nanofluids for spectral splitting with ORC and analyzed the system performance while regarding R1233zd as the working fluid of ORC and water/Ag solution as the nanofluid. They found that the electrical, thermal, and total efficiencies of the novel system were better than the traditional concentrating photovoltaic-thermal (CPV/T) system by 1.8%, 3.3%, and 5.1%, respectively. Joshua et al. [37] designed a SBS-CPV/T system based on a parabolic trough concentrator (PTC) with ORC. The system could transfer 24% and 31% of total solar energy into electricity and heat under the operating condition of maximum electricity generation. Ahmed et al. [33] proposed the combination of the SBS-CPV/T system and two-stage ORC to optimize solar cogeneration applications. The integrated system could produce 2.14 kWh/day/m^2 of electricity and 6.17 kWh/day/m^2 of heat, with a heat-to-power ratio of 2.83.

Currently, most existing studies focus on integrated SBS-CPV/T–ORC systems, while the combination of SBS-CPV/T with an organic flash cycle remains largely unexplored. As a special configuration of the ORC, the organic flash cycle (OFC) has smaller irreversible losses in the evaporator and is more suitable for high-temperature heat sources than the ORC [38,39]. Besides, most of the research [36,40] about the SBS-PV/T-ORC system now focuses on the part of heat exchanges between the heat recovery fluid and organic working fluid. This indirect coupling method effectively makes excellent use of the excess heat in the solar combined heat and power system to maximize energy utilization efficiency and power generation capacity. However, this coupling method limits the temperature range of the available heat sources because the ORC mainly has unique advantages and excellent performance in the field of medium and low-temperature heat sources [41,42]. In the current research, most solar combined heat and power systems can provide a high-temperature heat source for the subsequent power cycle by making simple improvements to the system structure [36,37,43]. To achieve higher system performance, the direct coupling is a promising application approach that enables the use of a nano-organic working fluid to combine the SBS-CPV/T and ORC. It not only effectively utilizes the high-temperature heat source produced by solar energy but also avoids exergy destruction caused by the heat exchanging process [44]. Existing research has demonstrated that the nano-organic working fluid shows performance improvement compared to traditional organic working fluids while being applied to the ORC [45]. Nevertheless, the accumulation of nanoparticles at the expander and the wear of related components caused by nanoparticles in the ORC configuration, which may occur over a long period of utilization, should be given special attention. The OFC configuration has great potential to address these challenges and achieve performance improvements. In the OFC configuration, the nano-organic working fluid will be separated into vapor phase and liquid phase, which means that nanoparticles are left in the liquid phase and mixed with the vapor phase in the condenser without entering the expander.

The present work designs a nano-organic working fluid to act as the main working fluid while combining OFC and PV/T systems. Then, the system will not need a heat exchanger between the nano-organic working fluid and the organic working fluid. Consequently, the exergy loss due to the heat transfer is reduced. A novel SBS-CPV/T-OFC is proposed. Thermodynamic parameters of four different SBS-CPV/T-OFC systems were analyzed. The effects of different kinds of organic working fluids on the system performance were examined to determine the most appropriate combination. The influence of critical parameters, such as the outlet temperature and flashing pressure, on the system efficiencies was also explored. A systematic comparative analysis of different OFC configurations, operating conditions, and working fluid selections was conducted to optimize overall system performance based on thermodynamic criteria. Meanwhile, this study proposed the novel coupling method between the heat source and OFC, and provided new insights into constructing a more efficient structure for a solar combined heat and power system.

2. System description

Fig. 1 shows the schematic configuration of the proposed SBS-CPV/T-OFC system. This novel system is mainly composed of an SBS-CPV/T collector based on the PTC device, the HCT part utilizing the nanofluid to realize the SBS, the OFC subsystem for achieving higher electricity production, and two heat exchangers (HE) to recycle waste heat for domestic heating of local users.

The solar radiation is reflected by the PTC and concentrated on the HCT, where the solar radiation can be filtered by the nanofluid so that the solar radiation at wavelengths that cannot be utilized by the PV cells is absorbed by the nanofluid. Then, the PV cells utilize the rest of the solar radiation for power generation. Meanwhile, the heated nanofluid is introduced into the OFC subsystem to generate electricity. During the process, the HTF is utilized to cool the PV cells for higher power generation efficiency [46,47] and is used for domestic heating in the HE2. Due to the excellent thermal stability and even performance within the medium temperature range [48], Therminol-55 is determined to act as the HTF in the system to recycle the waste heat of PV cells. As for the nanofluid (e.g., ZnO-R1336mzz(Z) nano-organic working fluid), its remaining thermal energy is recycled in the HE1 after completing the power generation of the OFC subsystem, with the same purpose of utilization. The parameters of the SBS-CPV/T-OFC system are demonstrated in Table 1.

2.1. The SBS-CPVT subsystem

The cross-sectional diagram of the SBS-CPV/T collector is shown in Fig. 2, and the material of the HCT is glass. An aluminum plate is considered the conductive plate (CP) to be located on the back of PV cells and to control the temperature of PV cells. Then, the HTF will absorb the heat from the CP for further domestic heating utilization. The outer surface of the HTF tube is covered by the thermal insulation material to minimize heat loss as much as possible.

In this work, the PV cells utilize Gallium Arsenide (GaAs) as the main material, which is beneficial to be applied in the SBS-CPV/T system because of its low efficiency-temperature loss coefficient (only 0.08%/°C [10]). In Fig. 3, it can be clearly observed that the spectral response of GaAs cells is within the wavelength range of 280 nm to 900 nm approximately [37]. Accordingly, the zinc oxide particle is selected to serve as the nanoparticle in the nanofluid due to its suitable spectral absorption range with the GaAs cell [50], rather than using silver nanoparticles, which would affect the spectral absorption range of the GaAs cells [51]. In this study, the mass concentration and the diameter of particles of ZnO nanoparticles are assigned as 22.3 ppm and 50 nm [50], and the solar irradiance is defined as 1000W/m^2 [33].

Table 1
The parameters of the SBS-CPV/T-OFC system.

Parameters	Symbols	Value	Ref.
Environmental Conditions			
Ambient Temperature, °C	T_0	20	[38]
Ambient pressure, kPa	P_0	101.325	[38]
Wind Speed, m/s	V_{wind}	5	[15,37]
SBS-CPV/T			
Width of PTC, m	Wid_{PTC}	3	[15,37]
Length of PTC, m	L_{PTC}	100	[15,37]
Area of PTC, m^2	A_{PTC}	300	[15,37]
Transmissivity of PTC	τ_{PTC}	0.00	[37]
Absorptivity of PTC	α_{PTC}	0.05	[37]
Reflectivity of PTC	ρ_{PTC}	0.95	[37]
Thickness of HCT, m	d_{HCT}	0.004	[33]
Inter diameter of HCT, m	$D_{in,HCT}$	0.03	[33]
Transmissivity of HCT	τ_{HCT}	0.95	[37]
Absorptivity of HCT	α_{HCT}	0.01	[37]
Reflectivity of HCT	ρ_{HCT}	0.04	[37]
Emissivity of HCT	ε_{HCT}	0.9	[37]
Temperature coefficient, %/K	β	0.08	[37]
Bandgap energy, eV/K	E_{bg}	1.43	[37]
Ideality factor	A'	1	[37]
Empirical parameter	k_1, b, z	0.03, 1.2, 0.98	[37]
Transmissivity of GaAs cell	τ_{PV}	0.00	[37]
Absorptivity of GaAs cell	α_{PV}	0.93	[37]
Reflectivity of GaAs cell	ρ_{PV}	0.07	[37]
Emissivity of GaAs cell	ε_{PV}	0.9	[33]
Thickness of Al Plate, m	d_{Al}	0.002	[33]
HTF channel Thickness, m	d_{HTF}	0.01	[33]
OFC			
Cooling water inlet temperature, °C	$T_{in,cw}$	20	[38]
Cooling water outlet temperature, °C	$T_{out,cw}$	30	[38]
Cooling water pressure, kPa	P_{cw}	101.325	[38]
Pinch point temperature difference, °C	ΔT_{pin}	10	[49]
Pump Isentropic Efficiency, %	η_{pump}	80	[38]
Expander Isentropic Efficiency, %	η_{exp}	85	[38]

2.2. The OFC configurations

As shown in Fig. 1, the nano-organic working fluid absorbs the heat in the HCT (2-3), and it is flashed into vapor and liquid states at a lower pressure compared to the pressure of point 3 (4-5/7) through the TV1 (3-4). The vapor drives the expander to do work (5-6), and the liquid after throttling (7-8) is mixed with the exhaust of the expander (6/8-9) before entering the mixer. The waste heat of the mixture is recycled in HE1 for heating (9-1, 14′-15′), subsequently, it will be pumped into the HCT for a new cycle (1-2).

The OFC mentioned above is defined as a basic OFC (BOFC) layout. The other three OFC configurations are also analyzed and compared in this work, as demonstrated in Fig. 4.

The ROFC (Regenerative organic flash cycle): Different from the

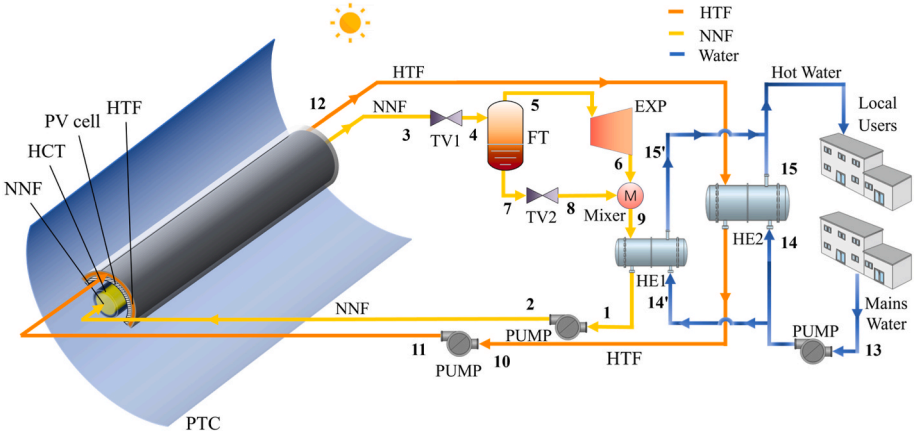


Fig. 1. Schematic configuration of SBS-CPV/T-OFC system.

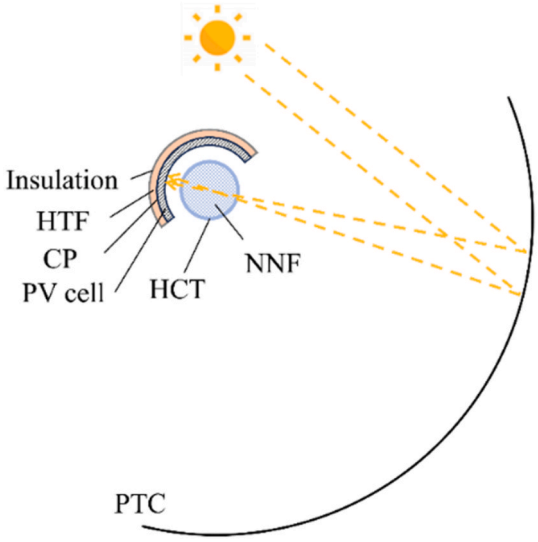


Fig. 2. Cross-sectional diagram of the SBS-CPV/T collector.

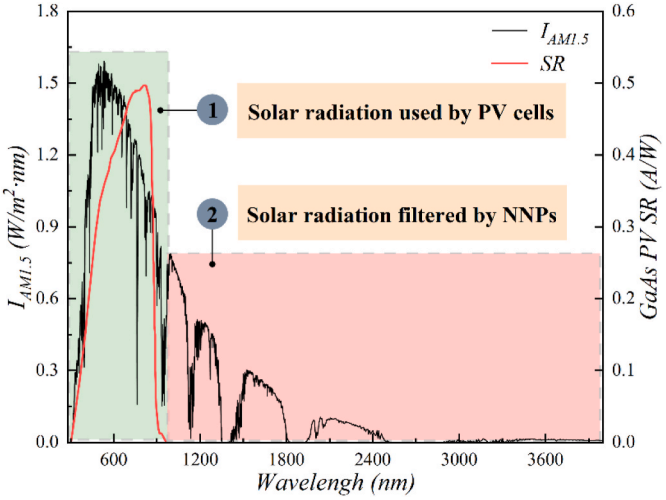


Fig. 3. Spectral irradiance of air mass 1.5 and spectral response of GaAs cells.

BOFC, the ROFC arranged the mixer after the condenser, as shown in Fig. 4(a). This configuration successfully decreases the heat load of the condenser and recovers most of the heat from the liquid working fluid. Therefore, the system acquires a higher inlet temperature.

The DOFC (Double-flashing organic flash cycle): Fig. 4(c) shows the configuration of the DOFC. In the DOFC, the working fluid is designed to flash twice. The liquid phase after the first flash operation enters the second flash tank, while the vapor phase, separated by the first flash tank, drives the high-pressure expander (HEXP). The other vapor phase, separated by the second flash tank, enters the low-pressure expander (LEXP) for power generation. The DOFC can utilize the thermal energy in the working fluid adequately, and it is instrumental in reducing unnecessary losses in the expansion process.

The RDOFC (Regenerative double-flashing organic flash cycle): As shown in Fig. 4(e), the RDOFC can be regarded as the combination of the ROFC and DOFC. It installs the mixer (the liquid phase and the vapor phase) after the condenser, in comparison with the DOFC. It combines the advantages of the two previous configurations while increasing the cost input of the total configuration.

In addition, the OFC is more suitable for the applications of intermediate- and high-temperature heat recovery compared to the ORC [42]. This work has selected seven widely used organic working fluids to serve as the base fluid of the nano-organic working fluid. Their critical temperatures are close to 170 °C and fall within the range of 140 °C to 200 °C. To reduce the restrictions on the structural materials of the system, the critical pressures of these organic working fluids range from 3 to 4 MPa, thereby increasing the flexibility in selecting working fluids to match the system construction. Moreover, three traditional working fluids and four new environmentally friendly working fluids are selected to meet the scientific rigor and environmental protection policies. The properties of these working fluids are shown in Table 2, which are derived from the database of REFPROP 10.0 and relevant research [52–54].

2.3. Assumptions

Some reasonable simplifications are conducive to reducing the computational load of the analysis of this SBS-CPV/T-OFC system while maintaining high calculation accuracy:

(1) The whole system is operating in a steady state, and instantaneous influences are ignored.
(2) The outer surface of the HTF tube is regarded as a completely adiabatic surface. Besides, the solar radiation absorbed by the Al plate and the HTF tube is neglected due to their extremely thin thickness, which means that the heat produced by the PV cells is absorbed by the heat transfer fluid, except for the necessary heat loss of the surface of the PV cell.
(3) The effects of different kinds of organic working fluids on the optical properties of the nanofluids are neglected. The optical properties of nanoparticles (ZnO) are the dominant factors that determine the transmissivity and absorptivity of the nanofluids.
(4) Pressure drop, heat loss, and friction loss in the tubes and components are ignored.

3. System models

3.1. Model of the SBS-CPV/T

In the present work, the AM1.5 spectral irradiance ($I_{AM1.5}$, as shown in Fig. 3) is integrated with respect to the wavelength (λ) to get the reference solar irradiance, $G_{AM1.5}$ [37],

$$G_{AM1.5} = \int_{280}^{4000} I_{AM1.5}(\lambda)\ d\lambda \tag{1}$$

Considering the transmissivity of nanofluid (τ_{nnf}, specific values of τ_{nnf} are derived from Ref. [50]) and glass tube (τ_{HCT}), the reflectivity of the PTC (ρ_{PTC}) and shadowless PTC region coefficient (γ), the solar radiation on the PV can be calculated as [37],

$$G_{PV} = \gamma \rho_{PTC} \tau_{HCT}^2 \frac{A_{PTC}}{A_{PV}} \int_{280}^{4000} \tau_{nnf}(\lambda)\ I_{AM1.5}(\lambda)\ d\lambda \tag{2}$$

where A_{PTC}/A_{PV} is the concentration ratio. Besides, solar radiation passes through the glass tube twice, so the τ_{HCT} needs to be considered twice. The region coefficient (γ) is assigned as 0.93 [37].

The performance of the PV cell is calculated in the following part. The dark saturation current can be written as [37],

$$J_{ds} = k_1 T_{std}^{3/z} \exp\left(\frac{-E_{bg}}{b k_{SB} T_{std}}\right) \tag{3}$$

where k_1, b, and z are empirical parameters. E_{bg}, k_{SB} and T_{std} are the band gap energy of the PV cell, the Stefan-Boltzmann constant, and the standard temperature (298.15 K). The short-circuit current is given by Eq. (4) [37],

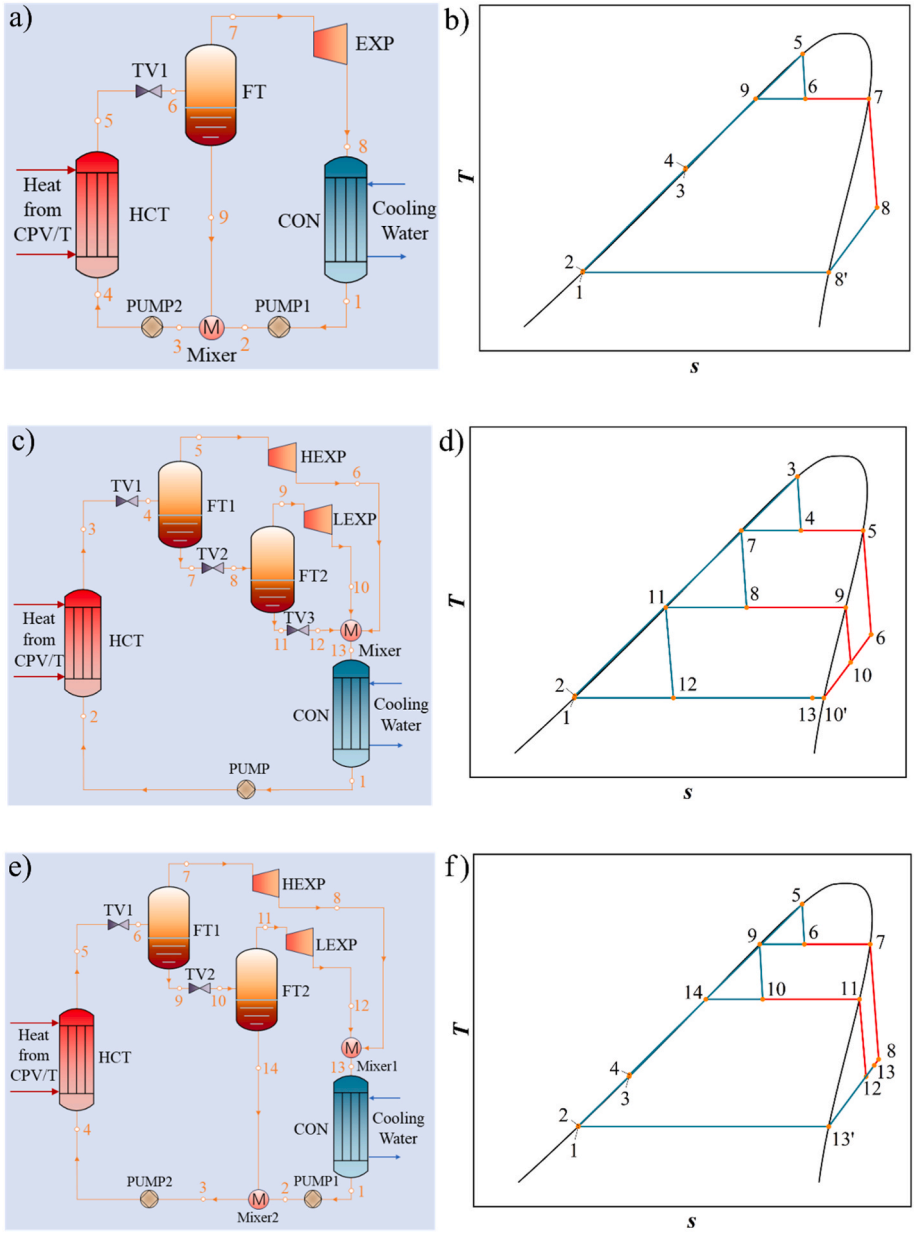


Fig. 4. Modified configurations and *T-s* diagrams of the OFC: (a-b) ROFC, (c-d) DOFC, (e-f) RDOFC.

Table 2
Properties of working fluids.

NO.	Fluid	T_c/°C	P_c/MPa	ODP	GWP_{100}	SG
1	Butene	146.1	4.01	0	20	A3
2	R601	196.6	3.37	0	20	A3
3	R365mfc	186.9	3.20	0	806	A1
4	R1224yd(Z)	155.5	3.33	~0	<1	A1
5	R1233zd(E)	166.5	3.62	~0	1	A1
6	R1234ze(Z)	150.1	3.53	0	1	A2
7	R1336mzz(Z)	171.3	2.90	0	2	A1

$$J_{sc} = \gamma \rho_{PTC} \tau_{HCT}^2 \frac{A_{PTC}}{A_{PV}} \alpha_{PV} A_{PV} \int_{280}^{4000} \tau_{nnf}(\lambda)\ I_{AM1.5}(\lambda)\ SR(\lambda)\ d\lambda \tag{4}$$

where α_{PV}, $SR(\lambda)$ are the absorptivity and spectral response of PV cells.

The open-circuit voltage is expressed as [37],

$$V_{oc} = \frac{A' k_{SB} T_{std}}{e} \ln\left(\frac{J_{sc}}{J_{ds}} + 1\right) \tag{5}$$

where e is the charge of an electron.

The electrical efficiency of the PV cell is defined as the ratio of the PV power to the solar radiation on the PV cell under standard conditions, which needs to be adjusted for the temperature effects [37],

$$\eta_{el,PV} = \frac{V_{oc} J_{sc} FF}{A_{PV} G_{PV}} (1 - \beta(T_{PV} - T_{std})) \tag{6}$$

where β is the temperature coefficient of the PV cell. T_{PV} is the temperature of the PV cell, and it is assigned as 373.15 K in this study [33]. As for *FF*, it is a filling factor and can be calculated by Eqs. (7)–(9) [55],

$$V_{th} = \frac{A' k_{SB} T_{std}}{e} \tag{7}$$

$$v_{oc} = \frac{V_{oc}}{V_{th}} \tag{8}$$

$$FF = \frac{v_{oc} - \ln(v_{oc} + 0.72)}{v_{oc} + 1} \tag{9}$$

Eq. (10) can be used to calculate the unutilized part of absorbed solar radiation by PV cell [37],

$$G_{PV,abs} = G_{PV} - \eta_{el,PV} G_{PV} \tag{10}$$

3.2. Model of the OFC

The OFC model is based on the laws of classical thermodynamics. The pressure of the flashing tank is the most sensitive parameter that affects the OFC performance, and it is optimized mainly under different working conditions of the OFC. Table 3 shows the main energy conversion equations of thermodynamic models of the OFC components.

3.2.1. Flashing process

Through the flashing after the TV, the working fluid is separated into liquid and vapor phases, respectively. The quality can be calculated from

$$x = \frac{h_4 - h_7}{h_5 - h_7} \tag{11}$$

where h_4, h_5 and h_7 represent the enthalpy of working fluid at state points 4, 5, and 7 in Fig. 1, respectively. The working fluid is in the saturated vapor state at state point 5 and the saturated liquid state at state point 7.

3.2.2. Exergy destructions

The exergy of the working fluid at different state points is written as,

$$E_i = m_i[(h_i - h_0) - T_0(s_i - s_0)] \tag{12}$$

where m_i, h_i and s_i are the mass flow rate, enthalpy, and entropy of the working fluid at the state point i. The T_0, h_0 and s_0 represent the ambient temperature, enthalpy, and entropy of the working fluid under ambient conditions. The specific values are from the database of Refprop 10.0 based on different operating conditions of OFC. The equations of exergy destruction in the different OFC components are listed in Table 4.

3.2.3. Efficiencies of the OFC

Based on the equations in Table 3, the net power of the OFCs can be calculated by,

$$W_{net} = W_{exp} - W_{pump} \tag{13}$$

where W_{exp} is the output power of the expander, and W_{pump} is the consumed power of the pump.

Then, the exergy efficiency of the OFCs can be calculated by,

$$\eta_{ex,OFC} = \frac{W_{net}}{E_{in,OFC}} \tag{14}$$

where $E_{in,OFC}$ is the total exergy brought into the OFC by the nanofluid in this study, given as,

Table 3
Energy conversion equations of the components in the OFC [38].

Components	Energy balance equations
HCT	$Q_{in,nnf} = m_{nnf}(h_{out,nnf}\text{-}h_{in,nnf})$
CON	$Q_{cw} = m_{cw}(h_{out,cw}\text{-}h_{in,cw}) = m_{nnf}(h_{in,nnf}\text{-}h_{out,nnf})$
EXP	$\eta_{exp}=(h_{in}\text{-}h_{out})/(h_{in}\text{-}h_{out,s})$; $W_{exp} = m_{nnf,\ vapor}(h_{in}\text{-}h_{out})$
TV	$h_{in} = h_{out}$
Mixer	$m_{in,vapor}h_{in,\ vapor} + m_{in,liquid}h_{in,\ liquid} = m_{nnf}h_{out,nnf}$
Pump	$\eta_{pump}=(h_{out}\text{-}h_{in})/(h_{out,s}\text{-}h_{in})$; $W_{pump} = m_{nnf}(h_{out}\text{-}h_{in})$

Table 4
The exergy destructions of the parts of OFCs [38].

Components	Exergy destruction
CON	$I_{con} = E_{in,cw,con}\text{-}E_{out,cw,con} + E_{in,nnf,con}\text{-}E_{out,nnf,con}$
Cooling water	$I_{cw} = E_{out,cw}$
EXP	$I_{exp} = E_{in,exp}\text{-}E_{out,exp}\text{-}W_{exp}$
TV	$I_{TV} = E_{in,TV}\text{-}E_{out,TV}$
FT	$I_{flash} = E_{in,flash}\text{-}E_{out,vapor,flash}\text{-}E_{out,liquid,\ flash}$
Mixer	$I_{mix} = E_{in,vapor,mix} + E_{in,liquid,mix}\text{-}E_{out,mix}$
Pump	$I_{pump} = E_{in,pump}\text{-}E_{out,pump} + W_{pump}$

$$E_{in,OFC} = E_{out,HCT} - E_{in,HCT} \tag{15}$$

where $E_{out,HCT}$ and $E_{in,HCT}$ represent the exergy of the working fluid at the outlet and the inlet of the HCT.

The thermal efficiency of the OFCs is regarded as the ratio of the net output power to the thermal energy absorbed by the working fluid ($Q_{in,nnf}$),

$$\eta_{th,OFC} = \frac{W_{net}}{Q_{in,nnf}} \tag{16}$$

3.3. Governing equations of the integrated system

3.3.1. Energy balance

The energy balance of the integrated system is expressed as [37],

$$Q_{in} = A_{PTC}G_{AM1.5} = Q_{in,HCT} + Q_{in,PV} + Q_{loss,PTC} \tag{17}$$

where $Q_{in,HCT}$ and $Q_{in,PV}$ represent the energy of the solar radiation reflected to the HCT and the PV cell, respectively, $Q_{loss,PTC}$ is the optical loss of the PTC. These three factors are calculated from Ref. [37],

$$Q_{loss,PTC} = (1 - \gamma\rho_{PTC})Q_{in} \tag{18}$$

$$Q_{in,PV} = A_{PV}G_{PV} \tag{19}$$

$$Q_{in,HCT} = Q_{in,gt} + Q_{in,nnf} + Q_{loss,gt,op} \tag{20}$$

where $Q_{in,gt}$ is the energy of the solar radiation absorbed by the glass tube, $Q_{in,nnf}$ represents the energy of the solar radiation absorbed by the nanofluid, and $Q_{loss,gt,op}$ is the optical loss due to the reflectivity of the glass tube. They can be calculated as [37],

$$Q_{in,gt} = \gamma\rho_{PTC}Q_{in}\alpha_{HCT} + \gamma\rho_{PTC}Q_{in}\tau_{HCT}\tau_{nnf}\alpha_{HCT} \tag{21}$$

$$Q_{in,nnf} = \gamma\rho_{PTC}\tau_{HCT}Q_{in}(1 - \tau_{nnf}) + \gamma\rho_{PTC}\tau_{HCT}Q_{in}\tau_{nnf}\rho_{HCT} \tag{22}$$

$$Q_{loss,gt,op} = \gamma\rho_{PTC}Q_{in}\rho_{HCT} \tag{23}$$

where ρ_{HCT} is the reflectivity of the HCT. Due to two transmissions of solar radiation through a glass tube, $Q_{in,gt}$ includes two parts of the energy of the solar radiation absorbed by the glass tube during the transmission process. Similarly, the nanofluid also absorbs the energy of solar radiation reflected by the glass tube in the second transmission, as shown in Eq. (22).

For the PV cell, the solar radiation reflected to the PV cell is divided into three parts [56],

$$Q_{in,PV} = Q_{loss,PV} + Q_{th,PV} + P_{el} \tag{24}$$

where $Q_{loss,PV}$ is the heat loss of the PV cell, $Q_{th,PV}$ is the heat absorbed by the HTF, and P_{el} is the electricity production from the PV cell. The following equations can be utilized to calculate the parameters above [56],

$$Q_{loss,PV} = Q_{loss,PV,em} + Q_{loss,PV,conv} + Q_{loss,PV,op} \tag{25}$$

$$Q_{\text{loss,PV,em}} = \varepsilon_{\text{PV}} \sigma A_{\text{PV}} \left(T_{\text{PV}}^4 - T_{\text{sky}}^4 \right) \tag{26}$$

$$Q_{\text{loss,PV,conv}} = h_n A_{\text{PV}} (T_{\text{PV}} - T_0) \tag{27}$$

$$Q_{\text{loss,PV,op}} = \rho_{\text{PV}} A_{\text{PV}} G_{\text{PV}} \tag{28}$$

$$P_{el} = \eta_{el,PV} A_{\text{PV}} G_{\text{PV}} \tag{29}$$

where $Q_{\text{loss,PV,em}}$, $Q_{\text{loss,PV,conv}}$, and $Q_{\text{loss,PV,op}}$ represent the emissive loss, convective heat loss, and the optical reflective loss from the surface of the PV cell, respectively. ε_{PV} is the emissivity of the PV cell, and σ is the Stefan-Boltzmann constant ($\sigma = 5.67 \times 10^{-8} W/(m^2 \cdot K^4)$). T_{sky} is the temperature of the distant sky ($T_{\text{sky}} = 0.0552\ T_0^{1.5}$). h_n is the convective heat transfer coefficient of the PV cell, and it is assigned as $10\ W/(m^2 \cdot K)$ [56].

As for the HCT, $Q_{\text{in,HCT}}$ is divided into three parts: the energy utilized in the OFC ($Q_{\text{in,OFC}}$), the heat loss of the HCT ($Q_{\text{loss,HCT}}$), and the optical loss of the HCT ($Q_{\text{loss,gt,op}}$).

$$Q_{\text{in,HCT}} = Q_{\text{in,OFC}} + Q_{\text{loss,HCT}} + Q_{\text{loss,gt,op}} \tag{30}$$

where $Q_{\text{loss,HCT}}$ include the emissive loss ($Q_{\text{loss,HCT,em}}$) and convective heat loss ($Q_{\text{loss,HCT,conv}}$) of the HCT, written as,

$$Q_{\text{loss,HCT,em}} = \varepsilon_{\text{HCT}} \sigma A_{\text{HCT}} \left(T_{\text{HCT}}^4 - T_{\text{sky}}^4 \right) \tag{31}$$

$$Q_{\text{loss,HCT,conv}} = h_K A_{\text{HCT}} (T_{\text{HCT}} - T_0) \tag{32}$$

where ε_{HCT} is the emissivity of the HCT. T_{HCT} is the temperature of the HCT. h_K represents the convective heat transfer coefficient of the HCT. The value of h_K can be calculated from,

$$h_K = \frac{1}{\frac{1}{h_{\text{in}}} + \frac{\log\left(\frac{R_{\text{out,HCT}}}{R_{\text{in,HCT}}}\right)}{2\pi k_g L_{\text{HCT}}} + \frac{1}{h_{\text{out}}}} \tag{33}$$

where $R_{\text{out,HCT}}$ and $R_{\text{in,HCT}}$ are the radius of the outer and inner of the HCT. k_g is the thermal conductivity coefficient of the glass tube, and is set as 0.68 [15,37]. h_{in} and h_{out} are the convective heat transfer coefficients of the inner and outer surfaces of the HCT, shown as [37],

$$h_{\text{in}} = \frac{k_{\text{nnf}} Nu_{\text{nnf}}}{D_{\text{in,HCT}}} \tag{34}$$

$$h_{\text{out}} = 4.5 + 2.9\ V_{\text{wind}} \tag{35}$$

where k_{nnf} is the thermal conductivity coefficient of the nanofluid, and Nu_{nnf} is the Nusselt number of the nanofluid. The effect of the ZnO nanoparticles on the thermodynamic properties of the nanofluid is neglected here. The thermodynamic properties of the nanofluid are mainly determined by the organic working fluid. The internal diameter of the HCT and the wind speed are expressed as $D_{\text{in,HCT}}$ and V_{wind}, respectively.

3.3.2. Efficiencies of the integrated system

Based on the equations above, the electrical efficiency of the integrated system can be calculated as [33],

$$\eta_{el} = \frac{W_{net} + P_{el}}{Q_{\text{in}}} \tag{36}$$

The thermal efficiency of the integrated system can be written as [33],

$$\eta_{th} = \frac{Q_{th,PV} + Q_{\text{cw}}}{Q_{\text{in}}} \tag{37}$$

where Q_{cw} is the heat energy recycled by the cooling water from the OFC for domestic heating.

3.4. System modelling

The proposed thermodynamic model has been implemented using both MATLAB and REFPROP to calculate the system performance parameters. In this work, the performance of the SBS-CPV/T-OFC system is evaluated by three main indicators: the η_{ex}, η_{th}, and η_{el}. The operating parameters that are most suitable for the system are found by iterative calculation. Fig. 5 shows the comprehensive calculation flow chart of the system. Initially, the performance parameters of the SBS-CPV/T are calculated based on the input parameters. Based on the data obtained above, the appropriate mass flow rate of nanofluid can be acquired through the iterative energy balance analysis of HCT. Then, the calculation of four different OFCs (BOFC, ROFC, DOFC, and RDOFC) is carried out using the data from the previous step. Moreover, different flashing pressures have a significant effect on the system performance. Finally, the system performance and parameters are analyzed and optimized under different operating conditions.

3.5. Model validation

The results from the work of Wang et al. [57] are adopted to validate the present thermodynamic model of the BOFC and ROFC system. Pentane serves as the working fluid of the OFC. The DOFC system is validated by the results from the study of Ho et al. [58]. Toluene is selected as the working fluid of the OFC. The comparison of results between the present work and previous research is shown in Table 5. It can be observed that there are only negligible errors between the predicted results and the literature data. Thus, the present model is reliable and accurate.

4. Results and discussion

In this section, the performance of the SBS-CPV/T-OFC system is discussed. The results are arranged as the effects of the flashing pressure on the OFC performance (4.1), the effects of the outlet temperature of the HCT in the OFC (4.2), the selection of the working fluids for the OFC (4.3), and the energy flow analysis of the SBS-CPV/T-OFC system (4.4). Based on the system models in Section 3 and parameters in Table 1, the performance of the SBS-CPV/T system can be acquired by numerical calculation. The SBS-CPV/T system achieves 35.369 kW of power output from electrical production and 84.590 kW of heat recovery for reutilization. Finally, the electrical efficiency of the SBS-CPV/T system is up to 11.79 %, and the thermal efficiency of the SBS-CPV/T system can reach 28.19 %.

4.1. Effects of the flashing pressure on the OFC performance

The flashing pressure of the working fluid after passing through the TV is one of the key parameters for the OFCs, which can influence the mass flow rate of the vapor separated from the working fluid and has a significant impact on the system performance. The effects of the flashing pressure are discussed and analyzed based on the four different OFC configurations. R1336mzz(Z) is selected as the working fluid of the OFC, and the outlet temperature of the HCT is assigned as 438.15 K in this section to avoid unnecessary influence on the performance of the OFCs.

Fig. 6 shows the effects of the flashing pressure (P_4) on the performance of the BOFC. It can be seen that the mass flow rate of nanofluid (m_{nnf}) is a constant value (0.4771 kg/s) while changing the P_4, since the temperature difference between the outlet temperature of the HCT and the inlet temperature of the HCT is stable during the changing process, which can be calculated by the system models mentioned in Section 3.2. The mass flow rate of the vapor (m_{vapor}) monotonically decreases with P_4 because less working fluid will be transferred into the vapor phase as P_4 increases. Consequently, the m_{vapor} driving the expander decreases, and

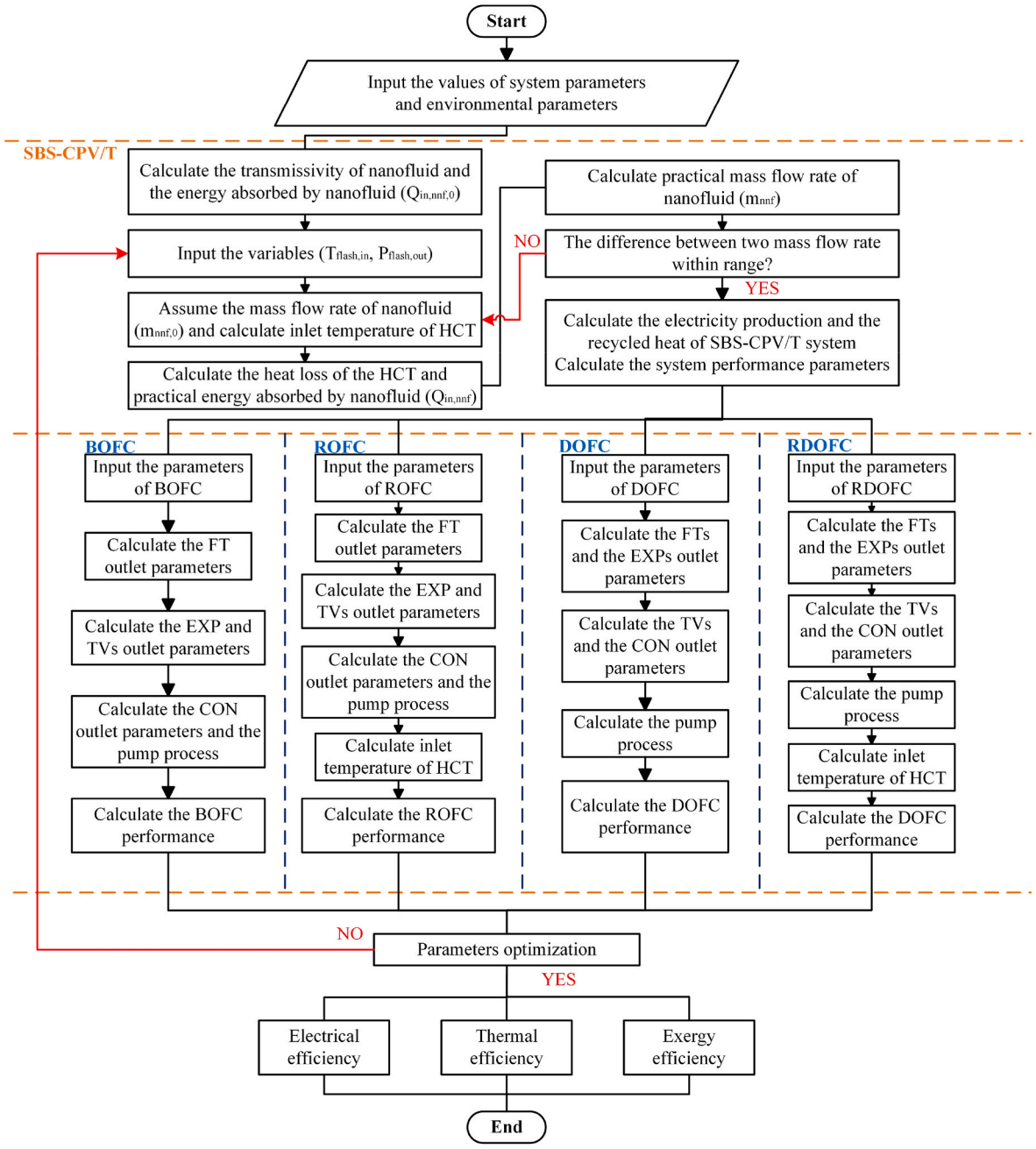


Fig. 5. Flow chart of the thermodynamic analysis of the SBS-CPV/T-OFC system.

the expander inlet pressure increases. As a result, the exergy efficiency and the thermal efficiency of the BOFC exhibit an initial increase followed by a decrease. When P_4 is 1012.18 kPa, they reach their maximum values simultaneously, with values of 43.92% for the exergy efficiency and 9.85% for the latter.

The effects of the flashing pressure (P_6) on the performance of the ROFC are shown in Fig. 7 (a). Based on the configuration of ROFC in Section 2, the difference between the BOFC and the ROFC is that the ROFC arranges the mixer after the condenser. In the ROFC, the inlet temperature of the HCT (T_4) is changing because the mass flow rate of the liquid (m_{liquid}) after flashing changes with P_6. Thus, the amount of heat recycled from the liquid phase is uncertain, which depends on the value of the P_6. However, the heat absorbed by the HCT is a stable value. As a result, the increment of the T_4, the growth of the heat loss of the HCT, and a decreasing trend of the energy utilized by the ROFC, while P_6 increases, are shown in Fig. 7 (b) comprehensively. While T_4 increases from 76.64 °C to 112.11 °C, the heat loss of the HCT increases by 20.55 %, and the energy utilized by the ROFC decreases by 8.50 %. Based on the analysis mentioned above, the changes in the performance parameters of the ROFC are reasonable in Fig. 7 (a). The m_{nnf} grows steadily, and the thermal efficiency of the ROFC continues to increase with a decreasing growth rate simultaneously. The thermal efficiency of the ROFC finally reaches 14.46 %, and the exergy efficiency of the ROFC achieves the peak value (50.215 %) with 1609.11 kPa of P_6.

As for the DOFC and RDOFC, it is seen that they add the second flash process compared to the BOFC and ROFC, respectively. Hence, the combined effect of the two flashing pressures on the performance of the DOFC and the RDOFC is discussed in detail, as shown in Fig. 8. The pressures on the corresponding state points are utilized to distinguish the first flashing pressure and the second flashing pressure of the two OFCs. P_4, P_8, P_6, and P_{10} represent the first flashing pressure of the DOFC, the second flashing pressure of the DOFC, the first flashing

Table 5
Comparison of results for the model validation.

Parameters	Ref. [57, 58]	Present work	Error (%)
BOFC			
Mass flow rate of working fluid, kg/s	7.92	7.92	0
Mass flow rate of vapor, kg/s	4.07	4.06	0.25
Mass flow rate of cooling water, kg/s	260.62	260.72	0.04
Net output power, kW	144.4	144.5	0.07
Outlet pressure of evaporation, kPa	1628	1628.06	0.004
Inlet pressure of expander, kPa	600	599.13	0.15
ROFC			
Mass flow rate of working fluid, kg/s	7.63	7.63	0
Mass flow rate of vapor, kg/s	3.94	3.95	0.254
Mass flow rate of cooling water, kg/s	160.80	161.17	0.23
Net output power, kW	142.07	142.83	0.535
Outlet pressure of evaporation, kPa	1628	1628.06	0.004
Inlet pressure of expander, kPa	596	594.34	0.279
DOFC			
Vapor quality of the first flashing	0.66	0.658	0.3
Operating temperature of the first flashing, K	494	494.08	0.016
Vapor quality of the second flashing	0.56	0.564	0.714
Operating temperature of the second flashing, K	410	409.87	0.032

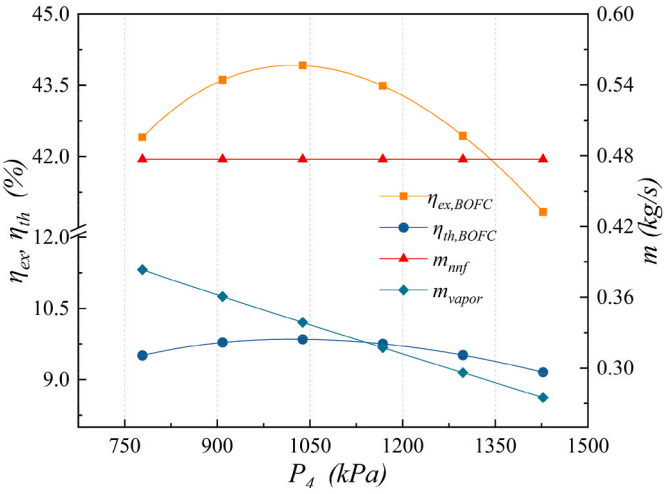


Fig. 6. Effects of the flashing pressure (P_4) on the performance of the BOFC.

pressure of the RDOFC, and the second flashing pressure of the RDOFC, respectively.

In Fig. 8(a, c, e), the exergy efficiency, the thermal efficiency, and the mass flow rate of the vapor of the DOFC are illustrated, respectively. With a given P_4, the exergy efficiency and the thermal efficiency of the DOFC show an increasing trend before their decrease, while P_8 increases. When P_4 is 1557.20 kPa and P_8 is 607.31 kPa, the exergy efficiency and the thermal efficiency of the DOFC reach their optimal value, 50.40 % and 11.30 %, respectively. As for the mass flow rate of the vapor (m_{vapor}) mentioned here, it is the sum of the vapor separated from two flashing processes. When P_4 remains constant, m_{vapor} shows a continuous downward trend while P_8 increases. m_{vapor} is 0.3626 kg/s under the condition of maximum exergy efficiency and thermal efficiency. Fig. 8(b, d, f) shows the exergy efficiency, the thermal efficiency, and the mass flow rate of the vapor of the RDOFC, respectively. It can be found that trends of these three performance parameters in the RDOFC are similar to those in the ROFC, while P_6 remains constant. As a result, when P_6 is 1842.69 kPa, and P_{10} is 1031.91 kPa, the exergy efficiency of the RDOFC is up to 53.52 %, and the thermal efficiency can reach 13.52 %. Meanwhile, m_{vapor} is 0.3655 kg/s.

Table 6 summarizes the optimal performance and operating parameters of the four OFC configurations with the optimal exergy efficiency. The results are based on the operating condition that the outlet temperature of the HCT is 438.15 K, and the working fluid is R1336mzz (Z). It can be seen that the RDOFC achieves the highest exergy efficiency, which is up to 53.52 %, representing an increase of 21.86% compared with the BOFC. Besides, the ROFC has the greatest thermal efficiency of 13.76%, which is only 0.24 % higher than the RDOFC. Thus, the performance of the RDOFC is the best in the four OFC configurations.

To explore what contributes to the high exergy efficiency of the RDOFC configuration, the comparison of exergy destruction of diverse parts between the BOFC and the RDOFC is demonstrated in Fig. 9. For the BOFC, the condenser and the flashing process are the main parts that cause exergy destruction, accounting for 19.01 % and 19.78 % of the total exergy flowing into the BOFC. As for the RDOFC, the two-stage expansion causes the slight growth of exergy destruction in the expander part (from 1474.62 W to 1839.59 W) and the mixer part (from 389.37 W to 1223.36 W). However, it vastly reduces exergy destruction in the flashing process from 3866.89 W to 1246.15 W and just accounts for 6.01 % of the total exergy flowing into the RDOFC, because the two-stage flashing process can reduce the degree of pressure drop and avoid the exergy destruction caused by the excessive pressure drop. Moreover, the process of heat recovery in the RDOFC reduces the difference between the inlet temperature and the outlet temperature of the HCT, so that the mass flow rate of nanofluid increases. As a result, the total exergy flowing into the RDOFC is more than that of the BOFC by 6.10%.

4.2. Effects of the outlet temperature of the HCT in the OFC

In Section 4.1, the influence of the flashing pressure on the performance of the OFC has been comprehensively investigated for a given outlet temperature of the HCT. In this section, the effect of the outlet temperature of the HCT is analyzed in detail. It is worth noting that the mass flow rate of the working fluid is determined by the difference between the inlet temperature and the outlet temperature of the HCT, which has a significant impact on the performance of the OFC.

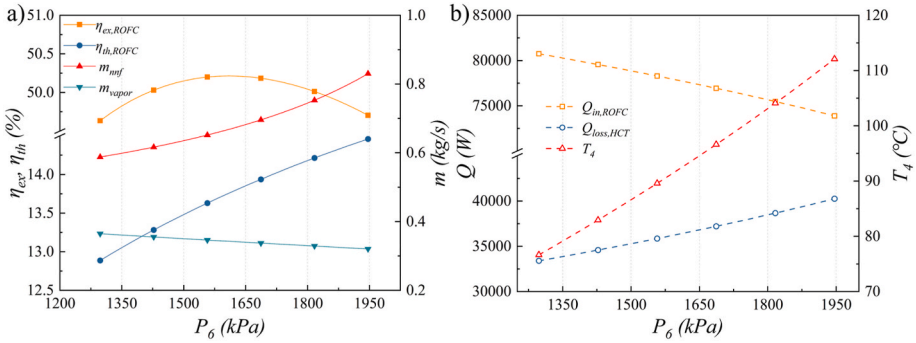


Fig. 7. Effect of the flashing pressure (P_6) on performance (a) and parameters variation (b) of the ROFC.

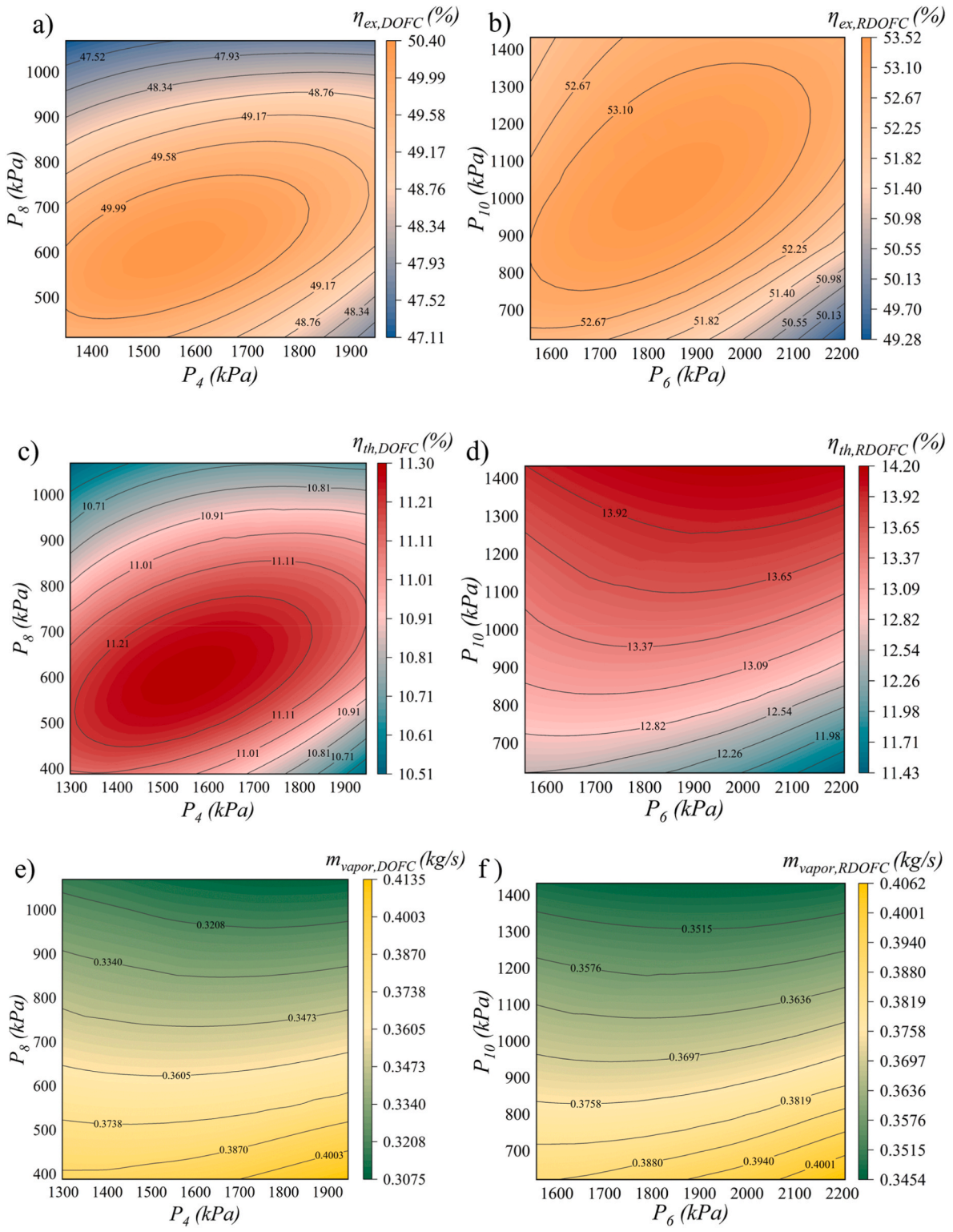


Fig. 8. Effect of the flashing pressures on the performance of the DOFC (a, c, e) and the RDOFC (b, d, f).

R1336mzz(Z) serves as the working fluid for the OFC. The outlet temperature of the HCT is limited to between 100 °C and 165 °C to avoid the outlet temperature of the HCT exceeding the critical temperature of the working fluid. In the present work, the outlet temperature of the HCT is controlled below 90% of the critical temperature, which is 154.17 °C for the R1336mzz(Z). In addition, the optimal parameters of each OFC configuration under the different outlet temperatures of the HCT are optimized to achieve the best exergy efficiency in this section.

As no heat recovery is considered in the BOFC and DOFC, the inlet temperature of the HCT in these two configurations is fixed, which is beneficial for determining the exact value of the mass flow rate of the working fluid with a given outlet temperature of the HCT (T_3). Fig.10 (a) and Fig.10 (b) illustrate the effects of T_3 on the performance of the BOFC and the DOFC, respectively. It can be seen that the changes in parameters in the BOFC are similar to those in the DOFC. While T_3 increases, the difference between the inlet temperature and the outlet temperature

Table 6
Comparison of optimal performance parameters in the four OFCs.

Parameters	BOFC	ROFC	DOFC	RDOFC
Exergy efficiency, %	43.92	50.21	50.40	53.52
Thermal efficiency, %	9.85	13.76	11.30	13.52
Flashing pressure 1, kPa	1012.18	1609.11	1557.20	1842.69
Flashing pressure 2, kPa	-	-	607.31	1031.91
Mass flow rate of working fluid, kg/s	0.4771	0.6680	0.4771	0.5582

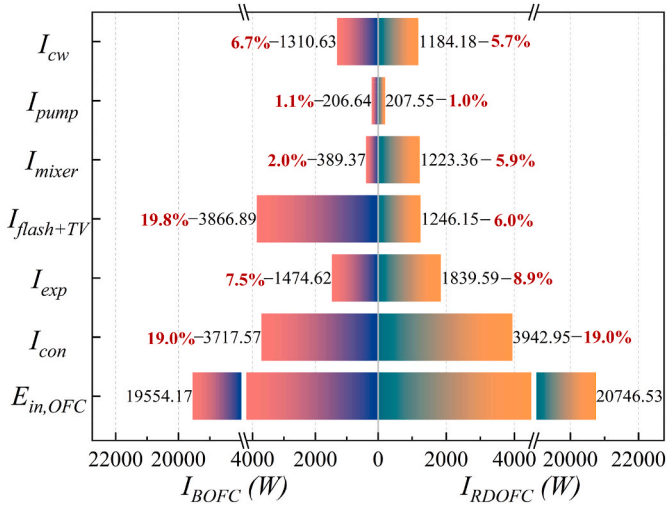


Fig. 9. Exergy destructions in the BOFC and RDOFC.

increases so that the mass flow rate of the working fluid shows a downward trend at a decreasing rate. However, the mass flow rate of the vapor remains almost stable because of the change in flashing pressure with the different values of T_3. Besides, the exergy efficiency of the OFC maintains a stable upward tendency, which is different from commonly reported results for OFCs [49]. It is caused by the lack of a heat exchanger on the evaporation side of the OFC in this study. Commonly, the exergy destruction of the heat exchanger on the evaporation side is a vital parameter utilized to optimize the performance of the traditional OFC configuration. It usually causes the exergy efficiency of the OFC to show a trend of rising before falling as T_3 increases.

For the ROFC, a distinct trend is observed while changing the outlet temperature of the HCT (T_5). Generally, the inlet pressure of TV remains a growing trend when T_5 increases, and there exists an optimal flashing pressure for each different T_5. However, when T_5 decreases in the ROFC, the flashing pressure gradually approaches the inlet pressure of the TV, leading to the pressure ratio (the flashing pressure to the inlet pressure of the TV) approaching 1.0 as shown in Fig. 11 (b). This phenomenon is caused by the excessive increase in the mass flow rate of the working fluid in the ROFC, which leads to a decrease in the proportion of the vapor driving the expander. Fig. 12 shows the changes in performance parameters in the ROFC with a definite T_5 (120 °C). It can be seen that the mass flow rate of the working fluid increases exponentially to ensure that the mass flow rate of vapor is sufficient for power production in the expander, so that the exergy efficiency of the ROFC asymptotically approaches a constant value. Meanwhile, most of the heat is retained in the liquid phase of the working fluid, which can increase the inlet temperature of the HCT. The difference between the inlet temperature and the outlet temperature of the HCT decreases, which causes an increase in the mass flow rate of the working fluid. Based on the analysis above, the performance of the ROFC represents idealized values within a lower temperature range, which represent idealized or non-physical results and cannot be achieved in practical applications. The detailed data about the effect of T_5 on the performance of the ROFC are illustrated in Fig. 11 (a).

As for the RDOFC, Fig. 13 demonstrates the effect of T_5 on the performance of the RDOFC, which shows the same trends compared to those of the BOFC and the DOFC. The exergy efficiency of the RDOFC can reach 53.52 % with 165 °C of T_5, which is better than that of the BOFC (43.92 %) and the DOFC (50.40 %). The thermal efficiency of the RDOFC is up to 13.52 %, which is 37.26 % higher than that of the BOFC.

4.3. Selection of the working fluids for the OFC

Fig. 14 illustrates the effects of the different working fluid selections on the exergy efficiency and net output power in four OFC configurations. The R365mfc shows better performance and a wider useable temperature range in the BOFC and the DOFC. When the outlet temperature of the HCT is 180 °C, the net output power (W_{net}) of the BOFC and the DOFC can reach 8472.09 W and 10578.90 W, respectively. The exergy efficiency of the DOFC is 5.61 % better than that of the BOFC, which is up to 52.29 %. Besides, the R601 is the most suitable of the seven selected working fluids in the ROFC and the RDOFC. It not only has a very wide temperature adaptation range, but also exhibits excellent operation performance within that range. The W_{net} of the RDOFC is 11988.54 W with 190 °C of the outlet temperature of the HCT, and its exergy efficiency can reach up to 56.12 %. With the same operating condition, the ROFC just achieves 11419.85 W of the W_{net} and 52.73 % of the exergy efficiency. It can be regarded as the most suitable organic working fluid in industrial systems with high technical standards and safety specifications. However, butene has the poorest overall performance among the seven working fluids in four OFC configurations, while it exhibits outstanding performance of net output power between 125 °C and 140 °C in the BOFC configuration.

However, due to the factors of environmental protection and climate change, the ozone depletion potential (ODP) and the global warming potential (GWP) of the working fluids should be considered in the selection of the working fluid. Taking all factors into consideration,

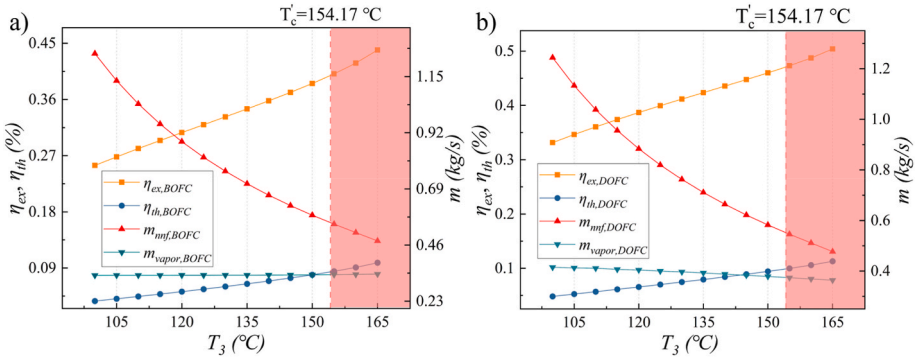


Fig. 10. Effect of the HCT outlet temperature (T_3) on performance of the BOFC (a) and DOFC (b).

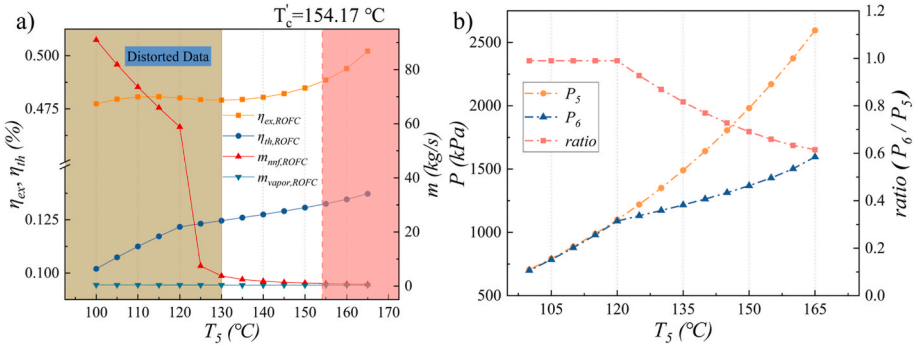


Fig. 11. Effect of the HCT outlet temperature (T_5) on performance (a) and parameters variation (b) of the ROFC.

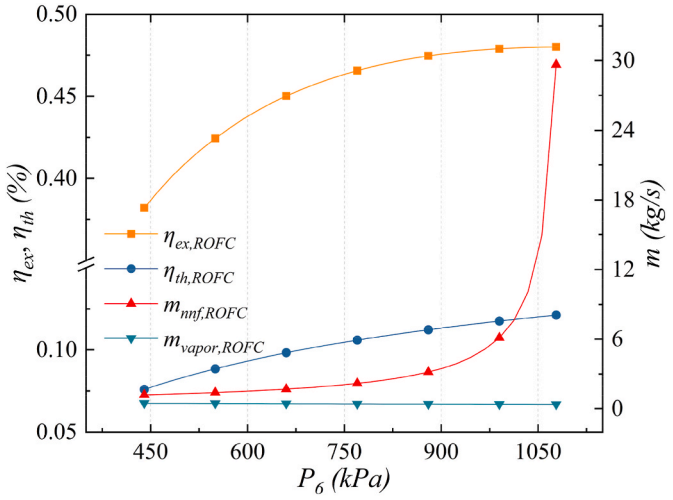


Fig. 12. Effect of the flashing pressure (P_6) on performance of the ROFC with T_5 (120 °C).

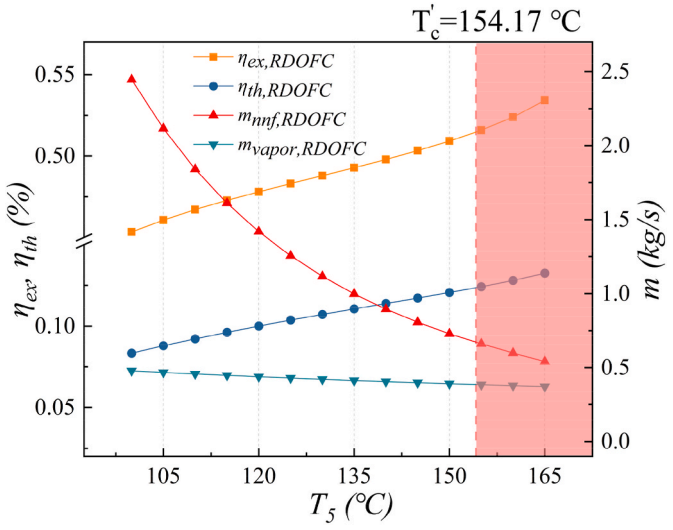


Fig. 13. Effect of the HCT outlet temperature (T_5) on the performance of the RDOFC.

R1336mzz(Z) is currently determined to act as the working fluid in the system. When the structural design of industrial systems and the research on the materials of key components continue to advance, R601 will become the most suitable choice among the seven working fluids after the environmental pollution risks during the operation and maintenance of the system have been eliminated. Based on the analysis above, when the outlet temperature of the HCT is set as 165 °C, the W_{net} of the RDOFC can reach 10998.89 W, which is more than 44.70 % of that of the BOFC (7601.19 W). The W_{net} of the DOFC and the ROFC are about 9854.86 W and 10692.08 W, respectively.

4.4. Energy flow analysis of the SBS-CPV/T-OFC system

According to the analysis and discussion mentioned above, the energy flow of the SBS-CPV/T-OFC system is discussed in this section, as shown in Fig. 15. The system parameters have been illustrated in Table 1, and the working fluid of the OFC is the R1336mzz(Z). The RDOFC is selected to serve as the OFC system in the integrated system based on the discussion in Sections 4.1 and 4.2. The outlet temperature of the HCT is assigned as 438.15 K to ensure the optimal performance of the RDOFC.

As illustrated in Fig. 15, the PV cell is the main power generation unit of the system, which amounts to 35.369 kW, accounting for 74.21 % of the total electricity output of the integrated system. The rest of the electricity production is generated by the high-pressure expander and the low-pressure expander of the RDOFC, with the values of 8.657 kW and 3.635 kW, respectively. Besides, the power input utilized for the power consumption of the pumps should also be considered, which is 1.182 kW. Consequently, the electrical efficiency of the system is up to 15.49 %. In addition, the total heat recycled from the integrated system is 155.604 kW, and the thermal efficiency of the system is 51.87 %. The heat transfer fluid recycles 84.590 kW of heat from the PV cell, and the remaining part is recycled from the nanofluid by the cooling water in the condenser.

The energy loss during the total process consists of optical loss and heat loss. The largest optical loss is caused by the PTC, with a value of 34.95 kW. The HCT part and the surface of the PV cell also cause the optical loss of 10.602 kW and 9.820 kW, respectively. Meanwhile, the heat loss of the HCT is up to 32.028 kW, accounting for 75.28 % of the total heat loss in this system. The rest of the heat loss is caused by the PV cell, which is about 10.517 kW.

Based on the previous thermodynamic analysis and energy flow chart, the findings demonstrate the remarkable potential of applying the SBS-CPV/T-RDOFC in practical engineering scenarios with high electrical efficiency (15.49%) and thermal efficiency (51.87%), confirming its strong competitiveness with other well-established combined heat and power systems in previous research. Table 7 shows the performance difference between the present study and previous works in detail.

4.5. Future work and challenges

Although the present study has systematically evaluated the thermodynamic performance of the proposed SBS-CPV/T-OFC cogeneration system, several theoretical and practical challenges remain to be addressed before its practical application. The main challenges are as

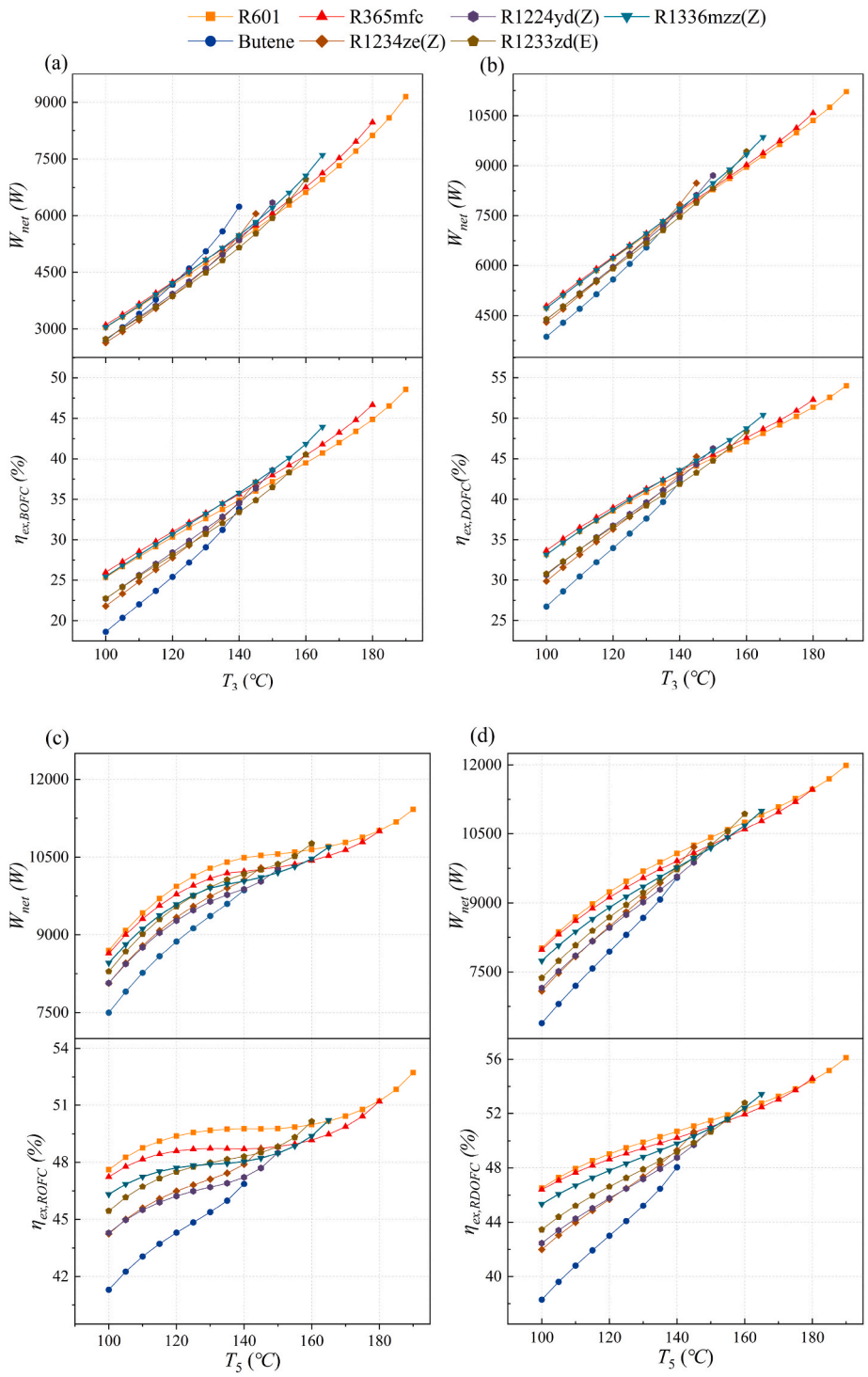


Fig. 14. Effect of different working fluids on the performance of four OFC configurations: (a) BOFC; (b) DOFC; (c) ROFC; (d) RDOFC.

follows:

(1) The long-term stability of nanofluid organic working fluids is a key concern, as nanoparticle agglomeration, sedimentation, and thermal or chemical degradation may alter thermophysical properties during prolonged operation. Future research should analyze maintenance cycles and optimize the design of the system structure.

(2) Variations in solar input and load conditions may induce dynamic instability. The advanced control strategies and dynamic modeling are expected to be proposed in future work.

(3) While the results provide useful insights into the potential of the novel system, the scalability of the system toward larger-scale applications involves additional considerations, such as component sizing and system integration.

(4) Economic feasibility and cost analysis are essential for the practical deployment of system. A techno-economic assessment is

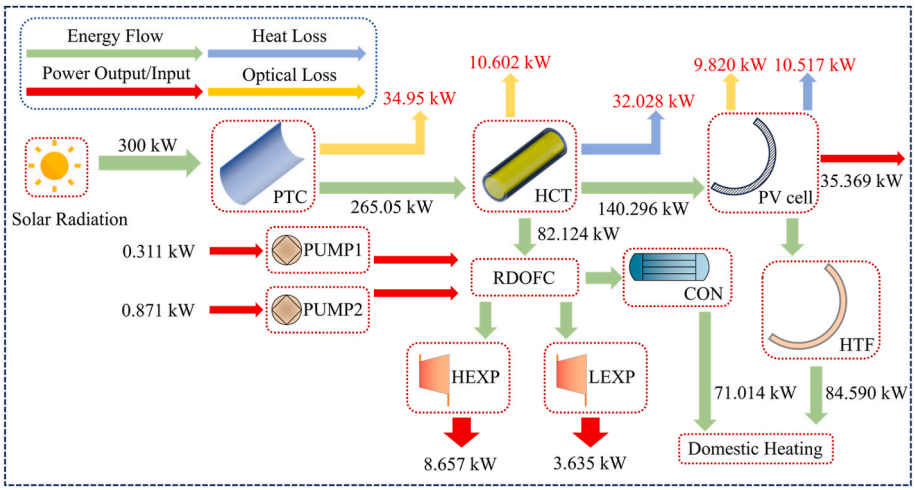


Fig. 15. Energy flow chart of the SBS-CPV/T-RDOFC system.

Table 7
Comparison of system performance with previous works.

Ref.	System/PV type/Working fluid	η_{el}	η_{th}
Present Study	SBS-CPVT-RDOFC/GaAs/R1336mzz(Z)	15.49%	51.87%
[33]	SBS-CPVT-TSORC/Si/R1233zd(E)	12.74%	36.75%
[37]	SBS-CPVT-ORC/GaAs/Toluene	23.6%	30.7%
[59]	PVT-ORC/a-Si/R1233zd(E)	26.85% overall efficiency	
[60]	PV/T-ORC/a-Si/R245fa	7.98%	57.5%
[61]	PV/T-ORC/a-Si/R12+RC318	7.82%	55%
[36]	NF-CPVT-ORC/InGaP-InGaAs-Ge/R1233zd	20.5% overall efficiency	

necessary for the SBS-CPV/T-OFC system to verify its practical application feasibility.

5. Conclusion

A novel SBS-CPV/T-OFC system is proposed in this work, which utilizes the ZnO nanoparticles to achieve spectral-beam-splitting and GaAs cells to act as PV cells. The thermodynamic model of the SBS-CPV/T-OFC system is established, and the influence of the system configurations and key parameters is explored comprehensively. The electrical efficiency, thermal efficiency, and exergy efficiency are applied to evaluate and optimize the system performance. The main findings are as follows:

(1) With the 1000 W/m^2 of solar irradiance at the parabolic trough concentrator, the SBS-CPV/T system achieves a power output of 35.37 kW from the PV cells and the heat recovery of 84.59 kW for further utilization by the OFC cycle and local heat users. The corresponding electrical efficiency of the SBS-CPV/T system can reach 11.79 % while the thermal efficiency is 28.19%. The energy loss in the SBS-CPV/T system consists of the optical loss of 55.37 kW and the heat loss of 42.54 kW, while the main optical loss is caused by the PTC, about 34.95 kW, and the main heat loss occurs at the HCT, about 32.03 kW.

(2) The outlet temperature of the HCT and the flashing pressure after the throttle valve are key parameters influencing the OFC operation and performance. Different from the traditional OFC system driven by the hot fluid of the heat source, the outlet temperature of the HCT in the present SBS-CPV/T-OFC system is limited by the critical temperature of the working fluid rather than the inlet temperature of the traditional heat source. The higher outlet temperature of the HCT leads to better performance of the OFC systems in terms of thermal efficiency and exergy efficiency. With the specified outlet temperature of the HCT, there is an optimal flashing pressure after the throttle valve where the OFC achieves the maximum exergy efficiency.

(3) Considering the thermodynamic performance, ODP, and GWP of the seven working fluid candidates, the R1336mzz(Z) is selected as a suitable working fluid. The RDOFC is recommended as the best configuration, which obtains an exergy efficiency of 53.52 % and 9.6 % higher than that of the BOFC with the working fluid of R1336mzz(Z) and the HCT outlet temperature of 165 °C. Under this condition, the electrical efficiency and thermal efficiency of the SBS-CPV/T-OFC system can reach up to 15.49 % and 51.87 %, respectively.

The high-cost investment in solar combined heat and power systems drives the process of optimizing system efficiency to achieve the best benefits and cost recovery. The next stage of research should comprehensively analyze the annual revenue of the system based on actual weather and natural environment, and develop a system dynamic response model that can adjust system parameters to deal with changes in actual application conditions. Besides, a comprehensive life cycle assessment should also be conducted to analyze the environmental impact and economic feasibility of the system compared to traditional cogeneration. These studies can effectively assist researchers and practitioners in improving the application and performance of SBS-CPV/T-OFC in the field of renewable energy.

CRediT authorship contribution statement

Yucheng Fang: Writing – original draft, Software, Investigation. **Chao Xu:** Validation, Methodology. **Jinliang Xu:** Visualization, Data curation. **Zheng Miao:** Supervision, Investigation, Conceptualization.

Declaration of competing interest

The authors declare that they have no known competing financial interests or personal relationships that could have appeared to influence the work reported in this paper.

Acknowledgment

The authors highly appreciate the support of the National Natural Science Foundation of China (No. 52476007).

Data availability

Data will be made available on request.

References

[1] Gao YZ, Wu DX, Dai ZF, Wang CL, Chen B, Zhang XS. A comprehensive review of the current status, developments, and outlooks of heat pipe photovoltaic and photovoltaic/thermal systems. Renew Energy 2023;207:539–74.
[2] Wang G, Zhang Z, Lin JQ. Multi-energy complementary power systems based on solar energy: a review. Renew Sustain Energy Rev 2024;199:41.
[3] Sarker SH, Amin S, Abrar N, Ehsan MM, Khan Y. Sustainable solar dish based CSP-fossil operated hybrid power plant with thermal energy storage utilizing triple extraction steam and organic Rankine cycles. Energy Conv Manag-X 2025;27:30.
[4] Khaled MM, Hossain T, Navid WU, Kamal MG, Ehsan MM, Khan Y, et al. Thermal analysis and dynamic attributes of a sustainable CSP-fossil hybrid power plant utilizing organic Rankine cycles for enhanced plant performance. Int J Thermofluids 2024;22:100696.
[5] Nanzeeba F, Baigh TA, Kabir A, Khan Y, Ehsan MM. Genetic algorithm-based optimization of combined supercritical CO_2 power and flash-tank enhanced transcritical CO_2 refrigeration cycle for shipboard waste heat recuperation. Energy Rep 2024;12:1810–35.
[6] Mathews I, Kantareddy SN, Buonassisi T, Peters IM. Technology and market perspective for indoor photovoltaic cells. Joule 2019;3(6):1415–26.
[7] Sirin C, Goggins J, Hajdukiewicz M. A review on building-integrated photovoltaic/thermal systems for green buildings. Appl Therm Eng 2023;229:25.
[8] Lu KG, Yu QW, Zhao B, Pei G. Performance analysis of a novel PV/T hybrid system based on spectral beam splitting. Renew Energy 2023;207:398–406.
[9] Zhao S, Li WZ, Abd El-Samie MM, Ju X, Xu C. Numerical simulation to study the effect of spectral division of solar irradiance on the spectral splitting photovoltaic/thermal system. Renew Energy 2022;182:634–46.
[10] Widyolar B, Jiang L, Winston R. Spectral beam splitting in hybrid PV/T parabolic trough systems for power generation. Appl Energy 2018;209:236–50.
[11] Han XY, Tu L, Sun Y. A spectrally splitting concentrating PV/T system using combined absorption optical filter and linear Fresnel reflector concentrator. Sol Energy 2021;223:168–81.
[12] Qiu HC, Liu H, Xia Q, Lin ZH, Chen C. A spectral splitting CPV/T hybrid system based on wave-selecting filter coated compound parabolic concentrator and linear Fresnel reflector concentrator. Renew Energy 2024;226:13.
[13] Yang N, Liu QF, Wang BW, Xuan J, Xing L. A novel PV/T system integrated with spectral beam filter: a comprehensive optical and thermodynamic study. Appl Therm Eng 2024;257:13.
[14] Liang HX, Wang FQ, Zhang D, Cheng ZM, Zhang CX, Lin B, et al. Experimental investigation of cost-effective ZnO nanofluid based spectral splitting CPV/T system. Energy 2020;194:9.
[15] Ni J, Li J, An W, Zhu T. Performance analysis of nanofluid-based spectral splitting PV/T system in combined heating and power application. Appl Therm Eng 2018;129:1160–70.
[16] Jiao Y, Xing MB, Estellé P. Efficient utilization of hybrid photovoltaic/thermal solar systems by nanofluid-based spectral beam splitting: a review. Sol Energy Mater Sol Cells 2024;265:17.
[17] Cui YL, Zhu J, Zoras S, Zhang JZ. Comprehensive review of the recent advances in PV/T system with loop-pipe configuration and nanofluid. Renew Sustain Energy Rev 2021;135:60.
[18] Kumar S, Chander N, Gupta VK, Kukreja R. Progress, challenges and future prospects of plasmonic nanofluid based direct absorption solar collectors-A state-of-the-art review. Sol Energy 2021;227:365–425.
[19] Salari A, Taheri A, Farzanehnia A, Passandideh-fard M, Sardarabadi M. An updated review of the performance of nanofluid-based photovoltaic thermal systems from energy, exergy, economic, and environmental (4E) approaches. J Clean Prod 2021;282:17.
[20] Liang HX, Wang FQ, Yang LW, Cheng ZM, Shuai Y, Tan HP. Progress in full spectrum solar energy utilization by spectral beam splitting hybrid PV/T system. Renew Sustain Energy Rev 2021;141:27.
[21] Sajid MU, Bicer Y. Nanofluids as solar spectrum splitters: a critical review. Sol Energy 2020;207:974–1001.
[22] Abdelrazik AS, Saidur R, Al-Sulaiman FA. Investigation of the performance of a hybrid PV/thermal system using water/silver nanofluid-based optical filter. Energy 2021;215:16.
[23] Han XY, Chen XB, Sun Y, Qu J. Performance improvement of a PV/T system utilizing Ag/$CoSO_4$-propylene glycol nanofluid optical filter. Energy 2020;192:12.
[24] Huang J, Han XY, Yao YP, Zheng J, Khosa AA. Optimization of plasmonic nanofluid filters for spectral splitting photovoltaic/thermal systems. Sustain Energy Technol Assessments 2024;65:7.
[25] Dashtbozorg A, Safarianbana B, Shanbedi M. Enhancing PV/T systems performance: a comprehensive study on MXene/methanol nanofluid in two-phase closed thermosyphons. Sol Energy Mater Sol Cells 2025;279:17.
[26] Huang J, Han XY. A novel integrated solar-driven system with Ag@SiO_2 nanofluid filters for generating hydrogen using seawater: parametric assessment and optimization. Int J Hydrogen Energy 2024;93:544–53.
[27] Huang MQ, Ren XJ, Tang G, Sun Q, Du M. Feasibility of realizing photothermal, photovoltaic, and radiative cooling with a flexible structure. Renew Energy 2024;236:16.
[28] Mahdi ZM, Al-Shamani AN, Al-Manea A, Al-zurfi HA, Al-Rbaihat R, Sopian K, et al. Enhancing photovoltaic thermal (PVT) performance with hybrid solar collector using phase change material, porous media, and nanofluid. Sol Energy 2024;283:22.
[29] Menon GS, Murali S, Elias J, Delfiya DSA, Alfiya PV, Samuel MP. Experimental investigations on unglazed photovoltaic-thermal (PVT) system using water and nanofluid cooling medium. Renew Energy 2022;188:986–96.
[30] Kazem HA, Al-Waeli AHA, Chaichan MT, Sopian K. Numerical and experimental evaluation of nanofluids based photovoltaic/thermal systems in Oman: using silicone-carbide nanoparticles with water-ethylene glycol mixture. Case Stud Therm Eng 2021;26:13.
[31] Liu HM, Zhu WB. Optimisation analysis by numerical simulation of adding internal fins in photovoltaic/thermal system based on Taguchi method. Appl Therm Eng 2025;266:18.
[32] Ma Y, Han XY, Chen Z, Khosa AA. Performance analysis of a nanofluid spectral splitting concentrating PV/T system with triangular receiver based on MCRT-FVM coupled method. Appl Therm Eng 2024;239:14.
[33] Elsayed A, Zhang BY, Miao Z, Liu GL, Xu C, Ju X. Exergetic and energetic parametric evaluation of integrated spectral beam splitting concentrated photovoltaic thermal and two-stage organic Rankine cycle system. Energy Convers Manag 2025;324:19.
[34] Loni R, Mahian O, Markides CN, Bellos E, le Roux WG, Kasaeian A, et al. A review of solar-driven organic Rankine cycles: recent challenges and future outlook. Renew Sustain Energy Rev 2021;150:32.
[35] Qyyum MA, Khan A, Ali S, Khurram MS, Mao N, Naquash A, et al. Assessment of working fluids, thermal resources and cooling utilities for Organic Rankine Cycles: State-of-the-art comparison, challenges, commercial status, and future prospects. Energy Convers Manag 2022;252:26.
[36] Rahbar K, Riasi A, Sangjoeei HKB, Razmjoo N. Heat recovery of nano-fluid based concentrating Photovoltaic Thermal (CPV/T) Collector with Organic Rankine Cycle. Energy Convers Manag 2019;179:373–96.
[37] Peacock J, Huang G, Song J, Markides CN. Techno-economic assessment of integrated spectral-beam-splitting photovoltaic-thermal (PV-T) and organic Rankine cycle (ORC) systems. Energy Convers Manag 2022;269:18.
[38] Huang BF, Fang YC, Miao Z, Xu JL. Thermodynamic analysis and optimization of the TI-PTES based on ORC/OFC with zeotropic mixture working fluids. J Energy Storage 2024;100:18.
[39] Miao Z, Xu JL, Zhang K. Experimental and modeling investigation of an organic Rankine cycle system based on the scroll expander. Energy 2017;134:35–49.
[40] Albaik I, Alamri YA, Elsheniti MB, Al-Dadah R, Mahmoud S, Ismail MA. Assessment of a novel multi-generation solar CPV/T system combining adsorption and organic rankine cycle subsystems. Sol Energy 2022;236:455–72.
[41] Yang CD, Yi FL, Zhang JY, Du GW, Yin W, Ma YH, et al. Towards high-performance of organic flash cycle through cycle configuration improvement: State-of-art research. Energy 2023;278:18.
[42] Ho T, Mao SS, Greif R. Comparison of the Organic Flash Cycle (OFC) to other advanced vapor cycles for intermediate and high temperature waste heat reclamation and solar thermal energy. Energy 2012;42(1):213–23.
[43] Wang K, Pantaleo AM, Herrando M, Faccia M, Pesmazoglou I, Franchetti BM, et al. Spectral-splitting hybrid PV-thermal (PVT) systems for combined heat and power provision to dairy farms. Renew Energy 2020;159:1047–65.
[44] Emadi MA, Chitgar N, Oyewunmi OA, Markides CN. Working-fluid selection and thermoeconomic optimisation of a combined cycle cogeneration dual-loop organic Rankine cycle (ORC) system for solid oxide fuel cell (SOFC) waste-heat recovery. Appl Energy 2020;261:20.
[45] Kosmadakis G, Neofytou P. Investigating the performance and cost effects of nanorefrigerants in a low-temperature ORC unit for waste heat recovery. Energy 2020;204:14.
[46] Guo XX, Zhai H, Wu ZH, Wang YY, Xie HQ. Higher conversion efficiency for combined systems with triple-junction GaAs photovoltaic cell and thermoelectric device. Energy Rep 2023;9:1426–35.
[47] Mohamed ET, Maka AOM, Mehmood M, Direedar AM, Amin N. Performance simulation of single and dual junction GaInP/GaAs tandem solar cells using AMPS-1D. Sustain Energy Technol Assessments 2021;44:11.
[48] Kadirgama G, Ramasamy D, Kadirgama K, Samylingam L, Aslfattahi N, Qazani MRC, et al. Characterization and machine learning analysis of hybrid alumina-copper oxide nanoparticles in therminol 55 for medium temperature heat transfer fluid. Sci Rep 2025;15(1):24.
[49] Chen LX, Hu P, Sheng CC, Zhang N, Xie MN, Wang FX. Thermodynamic analysis of three ejector based organic flash cycles for low grade waste heat recovery. Energy Convers Manag 2019;185:384–95.
[50] Liang HX, Wang FQ, Li D, Zhu J, Tan JY. Optical properties and transmittances of ZnO-containing nanofluids in spectral splitting photovoltaic/thermal systems. Int J Heat Mass Tran 2019;128:668–78.
[51] Han XY, Chen XB, Wang Q, Alelyani SM, Qu J. Investigation of $CoSO_4$-based Ag nanofluids as spectral beam splitters for hybrid PV/T applications. Sol Energy 2019;177:387–94.
[52] Chen HJ, Kim MH. Thermodynamic analysis and working fluid selection of a novel cogeneration System based on a regenerative organic flash cycle. Energies 2022;15(21):25.
[53] Wang MT, Hou YN, Chen PJ, Liu HW. Influence of thermophysical properties of working fluids on the performance of a double-stage organic flash cycle with an evaporator and an ejector. Energy 2025;328:14.
[54] Wang PL, Li QB, Liu C, Wang RQ, Luo Z, Zou P, et al. Comparative analysis of system performance of thermally integrated pumped thermal energy storage

systems based on organic flash cycle and organic Rankine cycle. Energy Convers Manag 2022;273:17.
[55] Singh P, Ravindra NM. Temperature dependence of solar cell performance-an analysis. Sol Energy Mater Sol Cells 2012;101:36–45.
[56] Han X, Xu C, Ju X, Du XZ, Yang YP. Energy analysis of a hybrid solar concentrating photovoltaic/concentrating solar power (CPV/CSP) system. Sci Bull 2015;60(4):460–9.
[57] Wang Q, Wu WF, Li DT, Wang JF, He ZL. Thermodynamic analysis and optimization of four organic flash cycle systems for waste heat recovery. Energy Convers Manag 2020;221:15.
[58] Ho T, Mao SS, Greif R. Increased power production through enhancements to the Organic Flash Cycle (OFC). Energy 2012;45(1):686–95.
[59] Dang GQ, Ren X, Gong L, Zhang YF, Liang JR, Li J, et al. A seasonally efficient cogeneration system based on medium-temperature PV/T-ORC. Energy 2025;316:17.
[60] Kutlu C, Li J, Su YH, Wang YB, Pei G, Riffat S. Investigation of an innovative PV/T-ORC system using amorphous silicon cells and evacuated flat plate solar collectors. Energy 2020;203:13.
[61] Ziapour BM, Afzal S, Ahmadi H. Compact PV/T-ORC hybrid system with zeotropic fluids and recirculated heat recovery for enhanced solar conversion. Energy Convers Manag 2025;346:19.